A novel interferometric method for the study of the viscoelastic properties of ultra-thin polymer films determined from nanobubble inflation

P. Chapuis,[1, a)] P. C. Montgomery,[2] F. Anstotz,[2] A. Leong-Hoï,[2] C. Gauthier,[1] J. Baschnagel,[1] G. Reiter,[3] G. B. McKenna,[4] and A. Rubin[1]

[1)] *University of Strasbourg, Institut Charles Sadron-CNRS/UPR22, 23 rue du Loess, BP 84047, 67037 Strasbourg, F-67034 Cedex 2, France*

[2)] *University of Strasbourg, Laboratoire des Sciences de l'Ingénieur, de l'Informatique et de l'Imagerie (ICube), Unistra-CNRS, 23 rue du Loess, 67037 Strasbourg, France*

[3)] *University of Freiburg, Institute of Physics, Hermann-Herder-Str. 3, 79104 Freiburg, Germany*

[4)] *Texas Tech University, Dept. of Chemical Eng., Box 43121, Lubbock, TX 79409-3121, USA*

(Dated: 3 August 2017)

Glass formation and glassy behavior remain important areas of investigation in soft matter physics with many aspects still not completely understood, especially at the nanometer size-scale. In the present work we show an extension of the "nanobubble inflation" method developed by O'Connell and McKenna[1] that uses an interferometric method to measure the topography of a large array of 5 μm sized nanometer thick films subjected to constant inflation pressures during which the bubbles grow or creep with time. The interferometric method offers the possibility of making measurements on multiple bubbles at once as well as having the advantage over the AFM methods of O'Connell and McKenna of being a true non-contact method. Here we demonstrate the method using ultra-thin films of both poly(vinyl acetate) (PVAc) and polystyrene (PS) and discuss the capabilities of the method relative to the AFM method, its advantages and disadvantages. Furthermore we show that the results from experiments on PVAc are consistent with the prior work on PVAc, while high stress results with the PS show signs of a new non-linear response regime that may be related to the plasticity of the ultra-thin film.

I. INTRODUCTION

An important material parameter is the glass transition temperature (T_g) below which a glass-forming material falls into the non-equilibrium glassy state characterised by solid-like behavior. Above T_g, the material is in the molten state. It is this property that has allowed significant advances in fuel saving, for example in the aeronautic and automotive industries, through the use of lighter polymer composites to replace metal parts. In bulk materials, T_g can be treated as a material parameter and is an important factor for structural design criteria and safe performance. On the other hand for ultra-thin polymer films, as the polymer is increasingly confined in a two-dimensional geometry, the T_g can vary as the film thickness decreases.[2,3] One approach to investigate this behavior is to make measurements of the dynamics (viscoelastic properties) of the materials confined to the nanometer thickness range. Some studies report that confinement and interfacial physics have different effects on the response of ultra-thin free-standing polymer films.[3,4] For example, preparing the film by spin-coating could result in an out-of-equilibrium state of the polymer chains.[5] Other studies[6–12] demonstrate that the viscoelastic response of ultra-thin polymer film is still not fully understood and can strongly depend on whether it is free-standing or supported due to non-negligible interactions with the substrate.

In this work, an experimental measurement cell based on the nanobubble inflation method developed by O'Connell and McKenna is used. In order to avoid film-substrate interactions, the technique consists of inflating a polymer film suspended over an array of 5 μm diameter holes in a Si grid wafer held in the setup. The creep compliance of the bubble is then determined by measuring the deformation as a function of time. Both PS and PVAc films of a few tens of nm thickness have been prepared by spin-coating from solution in toluene onto a Si wafer and manually transferring the film onto the perforated substrates using a water bath. Interference microscopy is used to measure the bubble growth as a function of time and, unlike the AFM methods,[1,13–16] is a true non-contact technique. While this technique has a very high axial sensitivity and allows single measurements revealing the curvature of the nanobubble over tens of nanometers, measurements made over long periods of time can be difficult to interpret due to the errors introduced by the different movements of the sample surface at the nanoscale.

In this paper some of the first solutions that we have developed to allow consistent measurements of film deformation using this novel non-contact technique are presented. Finally the first results on both PS and PVAc films are introduced and discussed.

[a)] pierre.chapuis@ics-cnrs.unistra.fr

II. NANOBUBBLE INFLATION

A. Method

Previous work by McKenna and co-workers on nanobubble inflation[1,13–16] used the tapping mode of AFM. This mode prevents the tip from damaging the fragile and soft free-standing films while the tip moves over the sample topography. However the film could be affected by the tip oscillations during the scan. To solve this possible trouble an interferometric microscopy experiment was used. Its advantage is principally the larger array of bubbles which can be probed and so the possibility to scale to larger bubbles if needed. Moreover its acquisition time takes only a few seconds (several minutes using AFM). The experiment was made close to $T_{\rm g}$ on 5 μm wide films. For films having a thickness close to the polymer coil size (ultra-thin), $T_{\rm g}$ depends strongly on the film properties and was estimated by the help of previous studies of Dalnoki-Veress *et al.*[17] Our experiment then applies the classical nanobubble inflation method,[18] where an ultra-thin free-standing film is deformed downward into the holes of a grid by capillary forces during an annealing process and is maintained by adhesion. When this sample is loaded onto the pressure cell, pressure from nitrogen gas is applied in order to inflate the nanobubbles.

B. Creep compliance calculation

Since the surface contour of each nanobubble can be measured, its radius of curvature R (small deflection) can be estimated by fitting the profile with a 2$^{\rm nd}$ order polynomial $z = f(x)$ (Fig. 1) and by applying the following expressions[19]:

$$R = 1/\kappa, \tag{1}$$

with:

$$\kappa = \frac{|z''|}{(1+z'^2)^{3/2}}, \tag{2}$$

where κ is the curvature. z' and z'' are the first and second derivatives of the 2$^{\rm nd}$ order polynomial $z(x)$.

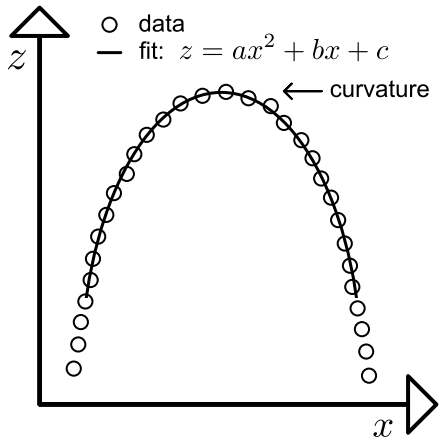

FIG. 1. Sketch of a nanobubble profile fitted by a second order polynomial $z = f(x)$.

Then both biaxial stress and biaxial strain, denoted respectively σ_{11} and ϵ_{11}, are given by:

$$\sigma_{11} = \sigma_{22} = \frac{PR}{2t_0}, \tag{3}$$

and

$$\epsilon_{11} = \epsilon_{22} = \frac{R\sin^{-1}(\frac{R_0}{R})}{R_0} - 1, \tag{4}$$

where P, t_0, R_0 and R are respectively the pressure, the film thickness, the hole radius and the radius of curvature.[1,18] Due to the change of the radius of curvature with time (t) as the nanobubble is inflated, the stress history has to be taken into account by applying the Boltzmann superposition principle:[16,20]

$$\epsilon(t) = \int_0^t \sigma(t-\xi)\left[\frac{dD(\xi)}{d\xi}\right] d\xi + D_g\sigma(t), \tag{5}$$

where $\epsilon(t)$, $\sigma(t)$, $D(t)$ and D_g are respectively the time-dependent biaxial strain, the time-dependent biaxial stress, the time-dependent biaxial creep compliance and the instantaneous glassy biaxial creep compliance. A modified KWW function is used to fit the data obtained for $\sigma(t)$ and $\epsilon(t)$ as:

$$\sigma(t) = \sigma_0 + \sigma_1 \exp\left[-\left(\frac{t}{\tau}\right)^{\beta_\sigma}\right], \tag{6}$$

and

$$\epsilon(t) = \epsilon_0 + \epsilon_1\left(1 - \exp\left[-\left(\frac{t}{\tau}\right)^{\beta_\epsilon}\right]\right), \tag{7}$$

where σ_0, σ_1, ϵ_0 and ϵ_1 are constant. τ is the retardation time, and β_σ and β_ϵ are the shape parameters for respectively the stress and strain curves. Using the trapezoidal method $\sigma(t)$ and $\epsilon(t)$ are estimated. Then $\Delta D(t)$ is determined by solving the equation (5), and finally the creep compliance $D(t)$ is calculated by adding step by step over time the $\Delta D(t)$ values.

III. EXPERIMENTAL DETAILS

A. Sample preparation

The polymer films were prepared by first making solutions of both polystyrene (PS, T_g = 100 °C) and poly(vinyl acetate) (PVAc, T_g = 30 °C): PS solutions between 1.3 % - 1.7 % (w/w) in toluene, with M_w^{PS} = 125 kDa and $PDI^{PS} = 1.05$, and PVAc solutions between 2.6 % - 3 % (w/w) in toluene, with $M_w^{PVAc} = 100$ kDa and $PDI^{PVAc} = 1.05$. The values of T_g (bulk) are taken from the literature. The solution was deposited on a square silicon wafer and then spin-coated at a speed ranging from 2000 rpm to 2500 rpm during a time ranging from 30 s to 60 s. The resulting film was transferred onto a bath (ultra pure water), where 4 perforated substrates had been deposited beforehand at the bottom. By removing carefully the water, the polymer film was moved down into the bath and finally deposited onto the substrates. These consist of micro sieve type filters from Aquamarijn Micro Filtration BV (Netherlands)[21] made by a nanostencil lithography method. A typical substrate, shown in Fig. 2, is seen to be a perforated square about $3 \times 3 \times 0.1$ mm^3 in size (split into 14 silicon nitride bands) mounted on a silicon support layer of $5 \times 5 \times 0.4$ mm^3 in size.

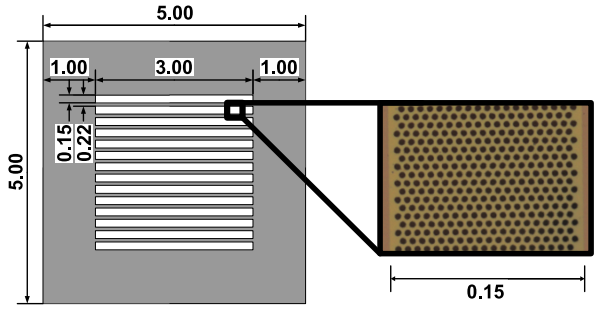

FIG. 2. Top view of a silicon square substrate[21] (5×5 mm^2, 0.4 mm thick) with 14 silicon nitride perforated bands. Focus: a piece of a perforated band where the holes, about 5 μm diameter, are closely spaced (optical microscope image).

After the deposition, the samples were allowed to dry overnight in air. Using an annealing process (1 h at T_g^{film} + 10 °C) the film bonds to the surface energies. The profile in Fig. 3 (AFM) shows a deflection for a 21 nm ± 5 nm thick PS film at 70 °C ± 2 °C. The deflection inside each hole depends on the annealing temperature and annealing time, and ranges from 200 nm − 250 nm. However during the experiment a waiting time of 1 hour is needed to reach thermal equilibrium at the setpoint temperature which leads to a further deflection of the film ranging from 10 nm − 20 nm during this time.

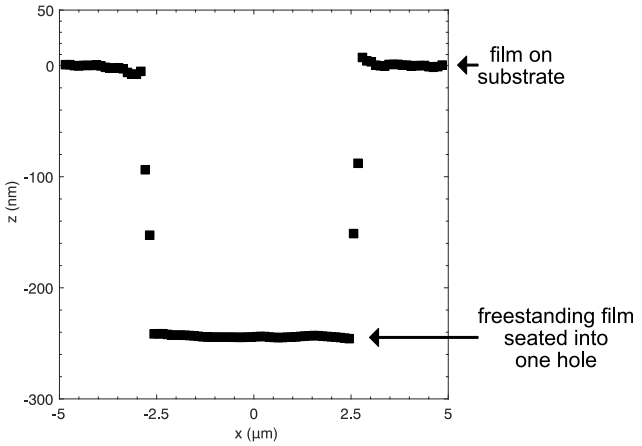

FIG. 3. A 240 nm deep deflection using AFM measurement of a 21 nm thick PS film at 70 °C. This process allows a good adhesion of the film inside the holes of the grid.

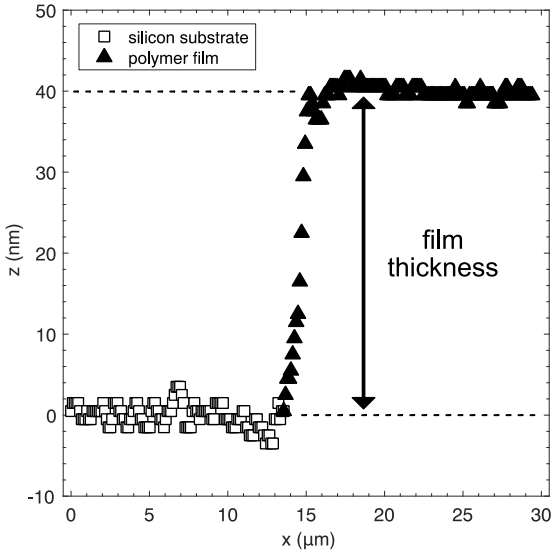

FIG. 4. An example of film thickness estimation (here a ∼ 40 nm thick PS film). The open squares and the filled triangles correspond respectively to the grid substrate and the polymer film.

Before fixing the sample into the pressure cell, the film thickness was estimated by making scored marks at the sample edges (on the grey area of the top view Fig. 2) using a single-edge razor blade. O'Connell and McKenna have demonstrated that this procedure only removes the polymer film and does not damage the silicon nitride

layer. Then, using the interference microscope the thickness was measured by probing near the scored marks. An example of one profile is shown in Fig. 4, where the difference between both plateaux corresponds to the film thickness. For a better accuracy an average over 10 profiles was performed, giving a standard deviation of ±5 nm due to the interferometric method.

B. Pressure and temperature controlled cell

A home-made apparatus (Fig. 5) was specially designed so as to be able to heat the film and to apply pressure. The cell is principally composed of an aluminium base and a sample holder, in teflon and aluminium. The pressure is provided by nitrogen gas from a bottle passing through a pressure regulator valve (Festo LRP-1/4-2,5) and finally arriving in the cell to push underneath the film located at its center. The setup allows a pressure range from 0 kPa − 400 kPa ± 5 kPa. The sample was placed at the center of the cell and was surrounded by a Peltier ring (Laird Technologies 71063-505) to be able to tune a setpoint temperature ranging from room temperature to 80 °C ±2 °C. A small thermocouple, put on the top of the Peltier element, and a temperature controller (Laird Technologies PR-59) regulates automatically the temperature using a computer interface (Laird Technologie SC_interface software). Another thermocouple was temporally placed onto an older perforated grid in order to calibrate the setup.

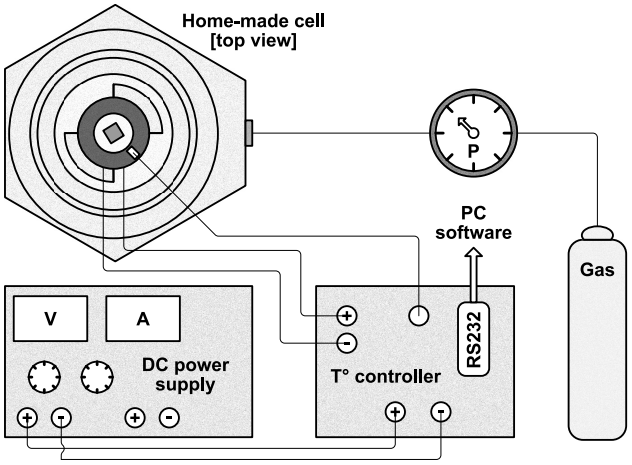

FIG. 5. Schematic drawing of the home-made experiment. The nitrogen gas passes through a regulator and then into the hexagonal stage. The Peltier ring is controlled by a temperature controller and a platinum resistance. The sample is symbolised by the grey square in the middle of the cell.

C. Interference microscopy technique

The measurements of the nanobubble deflection were made using a modified Leitz-Linnik interference microscope to be able to use the phase shifting technique (PSM).[22] This instrument is one of a family of new unlabelled nanoscopy techniques, consisting of far field optical microscopy that is used for extracting useful structural and physical information from nanostructures.[23] Coherence scanning interferometry (CSI), also known as white light scanning interferometry (WLSI), using polychromatic illumination, is more commonly used for the measurement of surface roughness and 3D microscopic surface structure.[24] In this technique, commonly used to characterise deep roughness, the white light fringes are scanned over the depth of the structure, and the fringe envelop peak is determined at each pixel in the image to reconstruct the surface topography.

The PSM technique, which uses monochromatic or quasi-monochromatic illumination, is used for the measurement of small roughness and surface structures, for example on the surface of optical components[25] and semiconductor materials.[26] Compared with AFM, while interference microscopy is limited in lateral resolution to about $\lambda/2$ (typically about 0.4 μm), it has the advantage of being non-contacting (no interaction with the sample), having a much wider field of view and a much faster acquisition time. A typical measurement of a static surface using PSM takes only several seconds.[27] Although the axial measurement sensitivity of interference microscopy can be better than 1 nm, achieving high accuracy at the nanoscale can be a challenge.[28] The present system (Fig. 6) includes two identical × 50 (NA = 0.85) objectives and an incandescent light source. A piezoelectric nanopositioner (PI Pifoc) controlled in a closed loop with a capacitive position sensor was used for the Z-scanning of the fringes over the sample depth. A color CCD camera (Basler avA1000-100gc) is used to acquire the images with a Giga Ethernet connection. The measurement system is controlled by a PC equipped with in-house developed LabVIEW based software (National Instrument, ver. 2014, 64 bits) combined with the IMAQ Vision module. The Linnik configuration of the interferometer (Fig. 6) has the advantage of being able to use high numerical aperture objectives, thus giving a better lateral resolution than the Mirau or Michelson type arrangements.[29]

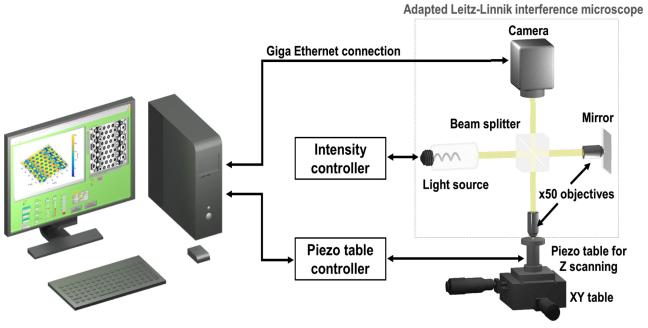

FIG. 6. Schematic layout of the measuring technique.[30]

A photo of the home-made cell placed under the microscope objective is shown in Fig. 7. The sample in the middle is surrounded by a Peltier ring and the temperature measurement is made using a platinum resistance (PRT).

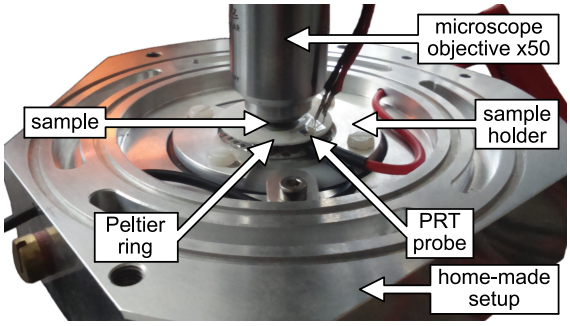

FIG. 7. Photo of the home-made pressure cell. The sample is located under the microscope objective and is surrounded by the Peltier ring. It is maintained by a holder, and a platinum resistance (PRT) allows temperature measurements.

The Linnik interferometer was adjusted first to produce high contrast fringes superimposed on the film surface by matching the path lengths of the two arms. During the pressure application each grid band is deflected, thus causing some curvature across the narrow width (Figs. 8 and 9). By using the PSM technique, due to the curved profile in the y-direction, the best way to obtain a good measurement was to orientate the fringes parallel to the grid bands (y-direction in Figs. 8 and 9).

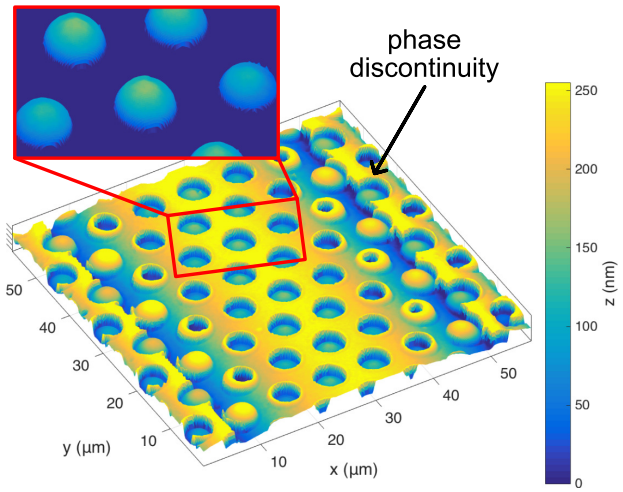

FIG. 8. 3D view of a nanobubble inflation inside the grid layer. For better clarity the inset shows a few nanobubbles by virtually hiding the grid. Phase discontinuities can be seen at two edges of the image.

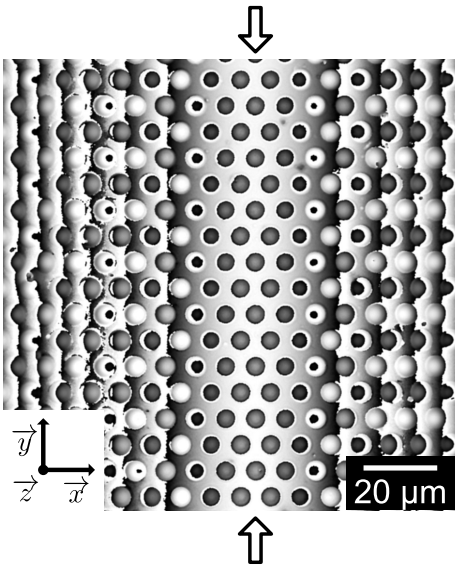

FIG. 9. Interferometric microscope image: deflected grid during the pressure. Only one line of bubbles (indicated by the open arrows) is not impacted by the grid curvature. Phase discontinuities are visible (dark/white steps).

In these first measurements, white light illumination was used, assuming a linear response for the phase measurements over the central black and white fringes. The basic phase stepping technique was used so as to stay as close as possible to the raw data and to avoid errors due to phase jumps (see discussion below on difficulties in nano-measurements "PSM algorithm for fringe interpretation"). The graph in Fig. 10 shows an example of the intensity I as a function of the phase ϕ, at one pixel (x, y) of the image. The green circles correspond to the intensities $(I_1, ..., I_5)$ measured at each step of $\delta\phi = \pi/2$ over a complete period of 2π for the five-phase step process.

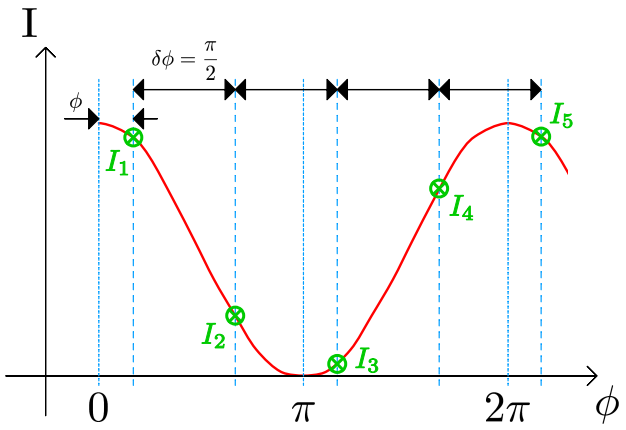

FIG. 10. Intensity I vs the phase ϕ. The green circles are the measured data, using the so-called five-phase step process of the PSM technique, over a period of 2π.

Using the data of the recorded intensities $(I_1, ..., I_5)$, the phase $\phi(x, y)$ for a pixel is given by:[31]

$$\phi(x,y) = \arctan\left[\frac{2(I_2(x,y) - I_4(x,y))}{2I_3(x,y) - I_5(x,y) - I_1(x,y)}\right]. \quad (8)$$

The "arctan" function in equation 8 can result in 2π phase jumps due to the periodicity of the fringes, which is a problem in our case because of the discontinuous shape of the samples. The algorithm used to make the phase measurement was a modified version of the 5-phase step algorithm (5 steps of $\pi/2$), together with image averaging of 5 frames, which is a good compromise between noise reduction and acquisition time. Due to the 2π phase discontinuities, the PSM algorithm only allows height measurements up to $\lambda_{eff}/2$ (< 290 nm at $\lambda_{eff} = 580$ nm). The effective wavelength λ_{eff} is longer than the real mean wavelength λ of the light due to the wide numerical aperture[32] (NA $= 0.85$), and is determined by directly measuring the fringe spacing. As both nanobubbles and grid bands were deflected together over time, a correction of the focus (along the z-axis) was needed before each acquisition in order to obtain the complete nanobubble shapes. Because the 2π phase discontinuities could not be successfully removed using the phase unwrapping routine available without producing image artefacts, the unwrapped phase was used to calculate the height. The reason for this is that the height at the step edge of the hole is very close to that of a phase discontinuity. Due to the curved profile, only one line of nanobubbles in the acquisition was useful (see the open arrows in Fig. 9) and was considered to be nearly flat. The height $z(x,y)$ of the surface at each pixel is expressed as:

$$z(x,y) = \frac{\phi(x,y)\lambda_{eff}}{4\pi}. \quad (9)$$

A single phase measurement, with averaging of each of the five images, takes ~ 5 s and the whole measurement procedure ~ 2 min, due to manual adjustments of the setup and storing of the results. The manual adjustment consists of refocusing in order to avoid the presence of a phase discontinuity in the measurement. Using the PSM technique a phase map of the sample was determined and then converted to height in order to give a contour map with nm axial sensitivity. After this typical acquisition a post-processing was required to reduce the camera noise (light 3×3 pixels median/low pass filtering).[22] In Fig. 11 a small deflection of a nanobubble (230 nm ± 5 nm thick PS film, 75 kPa ± 5 kPa, room temperature) in the glassy state is plotted before and after these successive steps of post-processing.

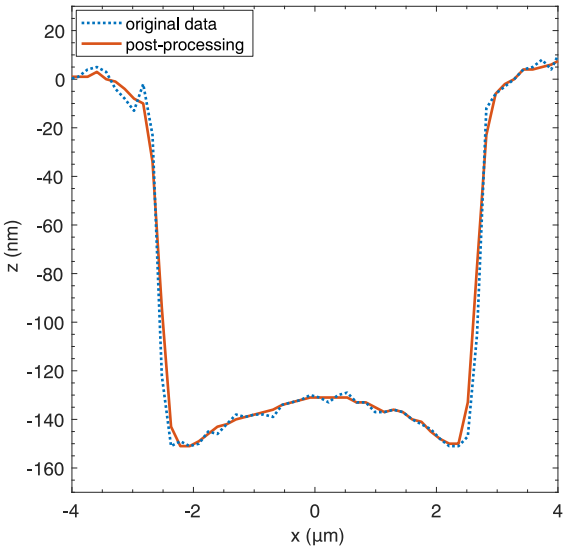

FIG. 11. Nanobubble profile before (dashed line) and after (solid line) median and low-pass filtering.

Measuring the nanobubble deformation at the nanoscale over a period of several hours is challenging, whatever the technique used. In the case of interferometric measurement at the nanoscale, for a single measurement of a relatively smooth surface sub-nm sensitivities are achievable.[27] However, in the presence of mechanical, thermal and pressure effects, measurements become harder due to different movements of the surface. In addition, there can be optical effects due to changes in illumination and phase across the image.

Several of these difficulties have already been overcome and some of the solutions developed are now described.

PSM algorithm for fringe interpretation – Due to various axial deformations of the sample, an envelope detection algorithm in white light would have been more appropriate for fringe interpretation. This is commonly used in the measurement of deep surface roughness[29] but with the drawback of having a limited axial sensitivity beteween 10 nm to 15 nm. This value can be improved by combining envelope detection with phase measurement.[33,34] However errors at the nanoscale can still appear in the case of the presence of steps (phase jumps) as in our samples leading to difficulties with phase unwrapping. The technique employed was first to align the array of holes symmetrically with the camera field of view and then to optimise the contrast and orientation of the fringes in the Linnik interferometer after phase stepping and acquisition. The unwrapped phase data was therefore used.

Effects of temperature variability – Before starting the experiment, waiting 1 h was needed to reach thermal equilibrium of both the sample cell and microscope objective. The change in temperature was observable by movement of the fringes, stabilised after

1 h, at the beginning of the heating cycle due to slight expansion of the perforated grid substrate.

Pressure effects – As the width of the grid bands is much smaller than their length (0.15 mm $\ll$ 3 mm), they were curved in the y-direction (Fig. 12) when under pressure. Therefore this leads to a semi-cylindrical shape of the perforated grid. The grid deflection reaches a maximum height h at its center, and this can be estimated by multiplying the number of phase discontinuities $n_{\rm ps}$ of one half of the grid surface by the phase length $l_{\rm p}$: $h = n_{\rm ps} \times l_{\rm p} \approx 7 \times 290$ nm ≈ 2 μm, for a sample loaded to 50 kPa at 70 °C and 100 min after starting the pressure. Regarding the support layer itself (about $5\times5\times0.4$ mm^3), plate theory[35] was helpful to conclude that its maximal deviation due to pressure could be neglected ($h \sim 45$ nm at the center for this example).

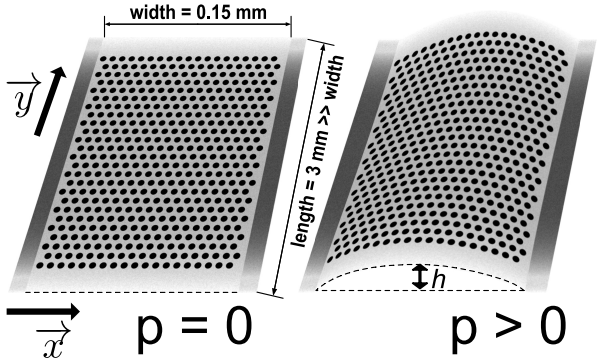

FIG. 12. Schematic layout of the deflection of one grid band following the y-axis due to pressure (the boundaries on the two width sides are neglected). The maximum level of deflection is denoted h.

A consequence of both grid and film deflections was the vertical drift over time of the overall position of the sample. This was solved by refocusing between measurements and also by writing a function in the controlling software in order to be able to adjust manually the fringes using the offset of the nanopositioner. Moreover, during the first 10 min the nanobubbles growth is fast and the present measurement procedure takes 2 minutes, which means that data acquisition was limited over this important initial period of deformation. Similar issues were found by McKenna and co-workers using the AFM nanobubble inflation method.

IV. MEASUREMENT OF THE VISCOELASTIC RESPONSE WITH TIME

A. Results on PVAc films

For this study the thickness of the film used was about 94 nm ± 5 nm and it was heated up to 40 °C ± 2 °C (which corresponds to 10 °C above $T_{\rm g}$). By applying a pressure of 25 kPa ± 5 kPa the nanobubble first grows over time and finally becomes stable. The profile in Fig. 13 shows the growth over a period of ~ 3 h measured by the proposed technique. Here the film deflection stays close to the membrane limit ($3t \approx 282$ nm), which could explain the results found for the creep compliance curve (Fig. 15).

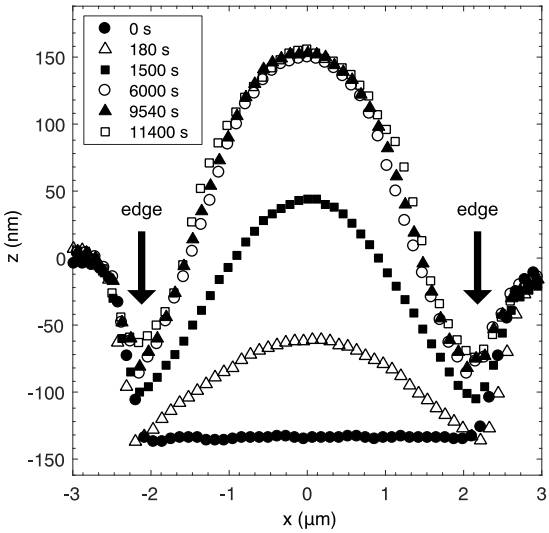

FIG. 13. PVAc ($M_{\rm w}^{\rm PVAc}$ = 100 kDa and $T_{\rm g}^{\rm bulk}$ = 30 °C) nanobubble growth vs time (PSM) at T = 40 °C.

The level $z = 0$ nm corresponds to the substrate. The edge position (black arrows on Fig. 13) of the nanobubble profiles appear to move upwards, thus leading to the following question: is this due to slipping of the polymer film at the edge or due to the measurement method? An investigation has suggested that this phenomenon is probably an artefact of the measurement technique near the the edge of the nanobubbles. Indeed, by taking 3 nanobubble profiles one after the other, the edge position of the bubble could sometimes move upwards and then downwards by a few tens of nm even though the position of the centre of the bubble remains at the same level in relation to the substrate. However due to pressure, the edge position is not allowed to move downward into the hole, which confirms the interpretation about artefacts of the measurement. This process, which takes less than 10 min, was made at a long time into the experiment (after 3 h at least) so as to ensure that the film height variations are negligible over a short period of time. Another explanation of this artefact could be the effects of diffraction at the edge linked to defocusing or due to non-linearities of the phase measurement using white light.

Using the method described in section II B, both the stress $\sigma(t)$ and strain $\epsilon(t)$ components (corresponding to the data in Fig. 13) were then calculated by using equations (3) and (4) and plotted in Fig. 14. The fits of $\sigma(t)$

and $\epsilon(t)$ were performed with equations (6) and (7). The parameters were $\sigma_0 = 1.14 \times 10^6$ Pa, $\sigma_1 = 3 \times 10^6$ Pa, $\beta_\sigma = 0.96$, $\epsilon_0 = 1.04 \times 10^{-4}$, $\epsilon_1 = 1.52 \times 10^{-2}$, $\beta_\epsilon = 0.9$. Since the precision of the first acquisition is highly impacted by the fast velocity of the nanobubble growth, we accordingly chose to ignore the first point ($t = 180$ s) for both fits. The strain increases as the polymer film creeps, that leads to a decrease in the radius of curvature of the nanobubbles and to a decrease of stress with time.[1,16,36,37]

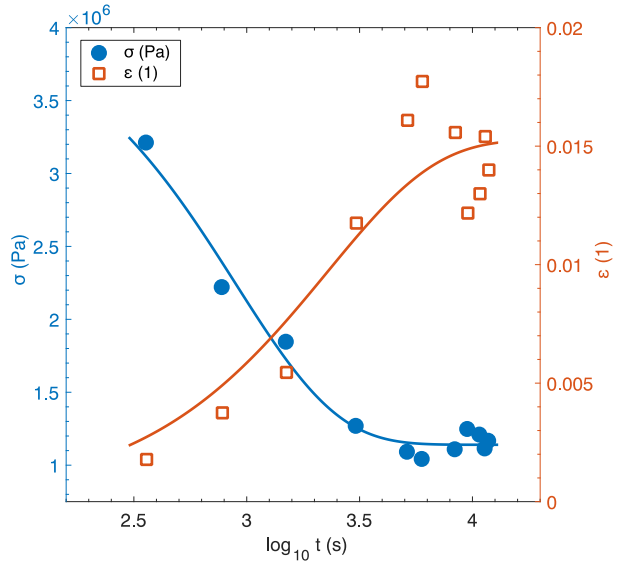

FIG. 14. σ and ϵ vs the logarithm of time corresponding to the data analysed from Fig. 13. The fits allow us to determine the creep compliance. The parameters were $\sigma_0 = 1.14 \times 10^6$ Pa, $\sigma_1 = 3 \times 10^6$ Pa, $\beta_\sigma = 0.96$, $\epsilon_0 = 1.04 \times 10^{-4}$, $\epsilon_1 = 1.52 \times 10^{-2}$, $\beta_\epsilon = 0.9$ and $\tau = 1500$ s.

Finally equation (5) was used to estimate the creep compliance of the polymer as a function of time (Fig. 15). To compute the creep compliance calculation, a Matlab program was written to perform an iterative procedure. The challenge here was to extrapolate the strain and stress curves to $t = 0$ s. As explained above the first acquisition could be performed a few minutes after the beginning of the experiment (starting point of the pressure). Thus the value of the creep compliance at $t = 0$ s, corresponding to the glassy compliance $D_g = \epsilon_0/\sigma_0$, could not be measured and has to be estimated using extrapolations, to $t = 0$ s, of both $\sigma(t)$ and $\epsilon(t)$ fits [using Eq. (6) and (7)]. As a consequence the first data points of the creep compliance $D(t)$ have higher uncertainty (see the error bars in Fig. 15). The creep compliance increases with time. The error bars correspond to the deviation of the creep compliance curve which depends on the fitting parameters of $\sigma(t)$ and $\epsilon(t)$. Master curves of McKenna and co-workers are also plotted.[16] Our 94 nm curve is not included between the 53 nm and the 152 nm master curves. Indeed our curve was plotted without taking into account the shift factors mentioned in the McKenna's article for the following reasons: they used a polydisperse PVAc while our PVAc is monodisperse. This might affect the breadth of the transition. Also, for PVAc, T_g is variously reported as being between about 30 °C and 40 °C, that would result in a large variation in the time scale of around a factor of 1000 depending on the estimated T_g of the film.

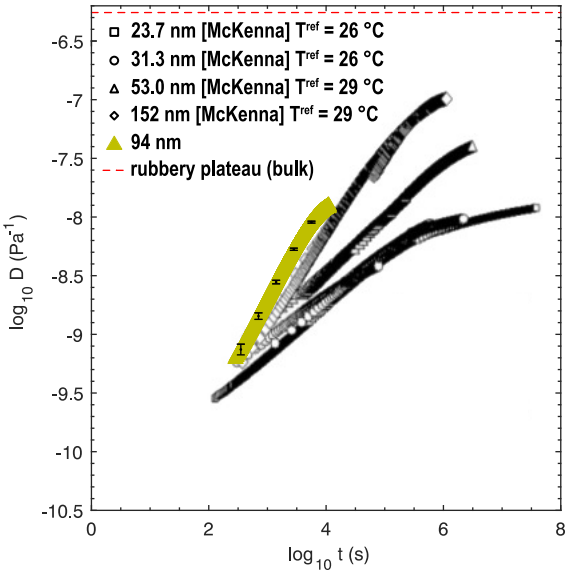

FIG. 15. Creep compliance vs logarithm of time for PVAc at 40 °C (yellow triangles). The error bars correspond to the deviation depending on the fitting parameters of $\sigma(t)$ and $\epsilon(t)$. Experimental results are compared to master curves taken from McKenna's work on PVAc.[16] The referenced temperatures are given in the legend. Reproduced with permission from J. Pol. Sc. Part B: Polymer Physics 46, 1952 (2008). Copyright 2008 American Institute of Physics.

An explanation for the difference regarding the creep response is the moisture level, which strongly interacts with PVAc material and could be different depending on the location of the experiment. Previous investigations have shown that a PVAc film at 26 °C with 40 % of humidity has a response $\approx$ 1.5 orders of magnitude shorter than the one at 14 % of humidity.[16] To reduce this effect, PS films were also investigated (see Sect. IV B).

After the experiment, the bubbles were close to the bending limit, that could also contribute to the difference in viscoelastic response between our results and those proposed by McKenna and co-workers.

B. Results on PS films

The growth in time of a 19 nm $\pm$ 5 nm thick PS film is plotted in Fig. 16. Both temperature and pressure applied were respectively about 70 °C $\pm$ 2 °C and 80 kPa $\pm$ 5 kPa. Here $z = 0$ nm corresponds to the

membrane height after the annealing process and before starting the pressure. Regarding the edge positions, the same behavior as for PVAc films is visible and is due to measurement artefacts. After a time close to 6000 s the contour of the nanobubble is modified. Indeed, contrary to the results shown for PVAc films, a radial inflection appears (see the dashed lines in Fig. 16). At the present time, the origin of this effect is not fully understood. One explanation maybe that the pressure is too high, so exceeding the yield point. In this case the polymer chains are too stressed and an irreversible state of the chains is started at this time.

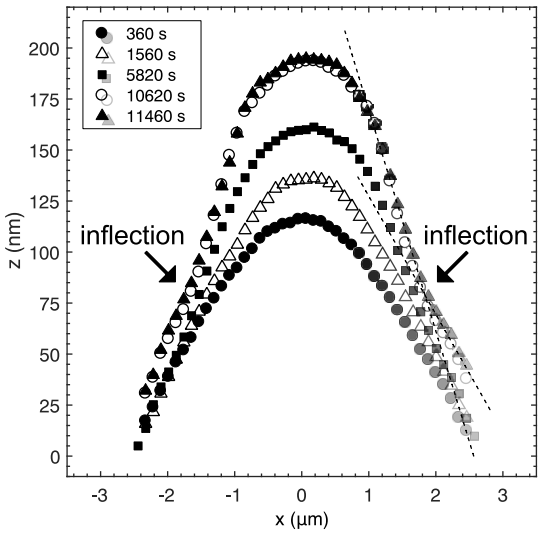

FIG. 16. PS ($M_w^{PS} = 125$ kDa and $T_g^{bulk} = 100$ °C) nanobubble growth vs time. Film thickness $t_0 = 19$ nm, temperature $T = 70$ °C. After ~ 6000 s a radial inflection appears. The intersection of the dashed lines emphasises this phenomenon. The data on the right have been opacified for better clarity.

By fitting the radius of each profile, the stress $\sigma(t)$ and strain $\epsilon(t)$ were estimated by taking into account their history (Fig. 17). Both quantities behave in the same way as for PVAc. However the acquisition was more difficult due to the small deviation of the PS nanobubbles. Using the interferometric measurement technique, the higher the film deflection (up to ~ 290 nm in z-axis) the better the precision during the acquisition. Because the deflection is smaller than in the PVAc study, the noise increases. This can be seen in Fig. 17. As a consequence, finding good fit parameters for the equations (6) and (7) was slightly tricky. Moreover, these equations could also be incomplete in this case because a non-linear model has to be applied in the computation.

Moreover the $\sigma(t)$ curve highlights that the material is close to the glassy state ($\sigma_0 \approx 10^7$ Pa). The polymer is harder than expected and has less ability to flow. Consequently the film could break under a too high pressure which would explain the radial inflection appearing after ~ 6000 s. This unexpected hardness points out that the T_g estimation method needs to be improved. Indeed as explained in Sect. II A the determination of T_g was performed by calculation using previous studies of Dalnoki-Veress and co-workers.[17] Adding the use of differential scanning calorimetry (DSC) should be helpful to reduce the error in T_g.

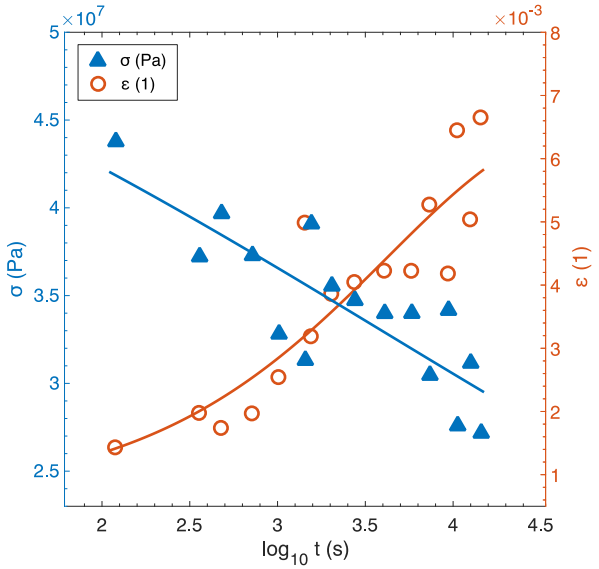

FIG. 17. σ and ϵ vs the log. of time. The strain is increasing as the polymer stress is decreasing. The parameters were $\sigma_0 = 1.456 \times 10^7$ Pa, $\sigma_1 = 5 \times 10^7$ Pa, $\beta_\sigma = 0.143$, $\epsilon_0 = 5.74 \times 10^{-4}$, $\epsilon_1 = 6.1 \times 10^{-3}$, $\beta_\epsilon = 0.54$ and $\tau = 4100$ s.

V. CONCLUSION AND OUTLOOK

The aim of this work was to extend the metrology for measuring the viscoelastic properties of polymer films with a true non-contact technique. The nanobubble inflation method[1] has been used in combination with interference microscopy for measuring the nanobubble profiles over time and provides a larger measurement area. An adapted pressure and temperature cell was especially developed for this study. Measuring nanodeformation over a period of several hours was challenging, due to deformations and drifts arising from the use of pressure and heating of the samples.

In this paper we have presented some of the first solutions developed to allow consistent interferometric measurements of film deformation. Creep compliance calculations for PVAc films were in accordance with the literature.[14] However the unexpected viscoelastic response for PS films suggests the need to take into account the non-linearity in our interpretation. An interesting way to continue this work would be to confirm and to investigate the emergence of the plastic

regime by applying an external stress from 0 Pa to high pressure, step by step in time, and by studying the transition between viscoelastic and plastic regimes (yield point). Moreover, improving the estimation of T_g becomes an important way to be able to fully compare our results with other studies.

The samples have been studied at the nanoscale. Improving the lateral and axial resolution of the Linnik interferometer is one of the next priorities. New tests have already been started by changing the white light of the interferometric microscope for a quasi-monochromatic blue light (a light-emitting diode). The first results are encouraging. The quasi-monochromatic light reduces artefacts of measurement which appeared using white light. The downside is that this light could be used only for nanobubble inflation up to $\sim$ 230 nm due to its shorter wave length. The measurement time could also be reduced to well below 2 min by automating the acquisition, processing and adjustment procedure. Future work will then involve the measurements of creep compliance as a function of different film properties, pressures, aging times and molecular weights. Moreover, the help of the Schapery model[38] could be useful for fully characterising our results regarding the non-linear viscoelastic behavior.

Finally, we plan to add a new feature in our experiment, consisting of moisture control. Indeed a special item for our home-made device has been especially developed to change the humidity rate in order to reduce errors on very moisture-sensitive polymers (like PVAc), and also to study its effects on the film properties.

ACKNOWLEDGMENTS

Financial support by the IRTG 1642 "Soft Matter Science" is gratefully acknowledged.

[1]P. A. O'Connell and G. B. McKenna, Review Of Scientific Instruments **78**, 1 (2007).
[2]J. L. Keddie, R. A. L. Jones, and R. A. Cory, Europhysics Letters **27**, 59 (1994).
[3]S. Lun, M. V. Massa, K. Dalnoki-Veress, H. R. Brown, and R. A. L. Jones, Phys. Rev. Lett. **94**, 127801 (2005).
[4]J. Baschnagel and F. Varnik, Journal of Physics: Condensed Matter **17** (2005).
[5]M. Chowdhury, P. Freyberg, F. Ziebert, A. C.-M. Yang, U. Steiner, and G. Reiter, Physical Review Letters **109**, 1 (2012).
[6]M. Alcoutlabi and G. B. McKenna, Journal of Physics: Condensed Matter **17**, 461 (2005).
[7]J. Wang and G. B. McKenna, Macromolecules **46**, 2485 (2013).
[8]J. Wang and G. B. McKenna, Journal of Polymer Science Part B: Polymer Physics **53**, 1559 (2015).
[9]J. Wang and G. B. McKenna, Journal of Polymer Science Part B: Polymer Physics of Applied Physics **51**, 1343 (2013).
[10]K. Dalnoki-Veress, J. A. Forrest, C. Murray, C. Gigault, and J. R. Dutcher, Physical Review E **63**, 1 (2001).
[11]J. A. Forrest, K. Dalnoki-Veress, and J. R. Dutcher, Physical Review E **56**, 5705 (1997).
[12]H. Bodiguel and C. Fretigny, The European Physical Journal E **19**, 185 (2006).
[13]S. Xu, P. A. O'Connell, G. B. McKenna, and S. Castagnet, Journal of polymer science Part B: Polymer Physics **50**, 466 (2011).
[14]P. O'Connell and G. McKenna, The European Physical Journal E **20**, 143 (2006).
[15]S. Xu, P. A. O'Connell, and G. B. McKenna, The Journal of Physical Chemistry **132**, 1 (2010).
[16]P. A. O'Connell, S. A. Hutcheson, and G. B. McKenna, Journal of Polymer Science Part B: Polymer Physics **46**, 1952 (2008).
[17]J. A. Forrest and K. Dalnoki-Veress, Advances in Colloid and Interface Science **94**, 167 (2000).
[18]A. E. Green, *Large Elastic Deformations* (Oxford University Press, London, 1970).
[19]M. P. D. Carmo, *Differential Geometry of Curves and Surfaces* (Prentice-Hall, 1976).
[20]E. Riande, R. Diaz-Calleja, M. Prolongo, R. Masegosa, and C. Salom, *Polymer Viscoelasticity: Stress and Strain in Practice* (CRC Press/ Marcel Dekker, New York, 2000).
[21]https://www.aquamarijn.nl, (Lastcheck 2016/11/28).
[22]P. C. Montgomery, D. Montaner, and F. Salzenstein, Proc. SPIE **8430** (2012).
[23]P. C. Montgomery, A. Leong-Hoi, F. Anstotz, D. Mitev, L. Pramatarova, and O. Haeberlé, Journal of Physics: Conference Series **682** (2016).
[24]P. de Groot, Advances in Optics and Photonics **7**, 1 (2015).
[25]O. Perrot, L. Guinvarc'h, D. Benhaddou, P. Montgomery, R. Rimet, B. Boulard, and C. Jacoboni, Journal of Non-Crystalline Solids **184**, 257 (1995).
[26]A. Benatmane, P. C. Montgomery, E. Fogarassy, and D. Zahorski, Applied Surface Science **208-209**, 189 (2003).
[27]J. Schmit, J. Reed, E. Novak, and J. K. J. Gimzewski, Journal of Optics A: Pure and Applied Optics **10** (2008).
[28]P. C. Montgomery, M. Guellil, P. Pfeiffer, B. Serio, F. Anstotz, L. Pramatarova, and S. Roques, Journal of Physics: Conference Series **558** (2014).
[29]P. de Groot, *Handbook of Optical Metrology: Principles and Applications* (CRC Press, Boca Raton, 2015).
[30]P. C. Montgomery, P. Chapuis, A. Leong-Hoï, F. Anstotz, A. Rubin, J. Baschnagel, C. Gauthier, G. Reiter, and G. B. McKenna, Journal of Physics: Conference Series **IOP Publishing** (2017).
[31]P. Hariharan, B. F. Oreb, and T. Eiju, APPLIED OPTICS **26**, 2504 (1987).
[32]C. J. R. Sheppard and K. G. Larkin, APPLIED OPTICS **34**, 4731 (1995).
[33]A. Harasaki and J. C. Wyant, Appl. Opt. **39**, 2101 (2000).
[34]P. C. Montgomery, F. Salzenstein, D. Montaner, B. Serio, and P. Pfeiffer, Proc. SPIE **8788** (2013).
[35]I. Danaila, P. Joly, S. M. Kaber, and M. Postel, *Introduction au Calcul Scientifique par la Pratique*, ISBN: 2-10-0048709-4 (Dunod, 2005).
[36]P. A. O'Connell and G. B. McKenna, Scanning **30**, 184 (2008).
[37]P. A. O'Connell and G. B. McKenna, Science **307**, 1760 (2005).
[38]R. Schapery, Polymer Engineering and Science **9**, 295 (1969).